arXiv:1704.02812v1 [cond-mat.mtrl-sci] 10 Apr 2017

Ordering versus irradiation effects in high-entropy alloys: Steady-state conditions in a driven system

Leonie Koch,[1,*] Fredric Granberg,[2] Tobias Brink,[1] Karsten Albe,[1] Flyura Djurabekova,[2,3] and Kai Nordlund[2]

[1] *Fachgebiet Materialmodellierung, Institut für Materialwissenschaft, TU Darmstadt, Jovanka-Bontschits-Straße 2, D-64287 Darmstadt, Germany*

[2] *Department of Physics, P.O. Box 43, FIN-00014 University of Helsinki, Finland*

[3] *Helsinki Institute of Physics, P.O. Box 43, FIN-00014 University of Helsinki, Finland*

(Dated: April 11, 2017)

We study order transitions and defect formation in a model high-entropy alloy (CuNiCoFe) under ion irradiation by means of molecular dynamics simulations. Using a hybrid Monte-Carlo/molecular dynamics scheme a model alloy is generated which is thermodynamically stabilized by configurational entropy at elevated temperatures, but partly decomposes at lower temperatures by copper precipation. Both the high-entropy and the multiphase sample are then subjected to simulated particle irradiation. The damage accumulation is analyzed and compared to an elemental Ni reference system. The results reveal that the high-entropy alloy—independent of the initial configuration—installs a certain fraction of short-range order even under particle irradiation. Moreover, the results provide evidence that defect accumulation is reduced in the high-entropy alloy. This is because the reduced mobility of point defects leads to a steady state of defect creation and annihilation. The lattice defects generated by irradiation are shown to act as sinks for Cu segregation.

I. INTRODUCTION

High-entropy alloys (HEAs) constitute a relatively new class of materials, which have recently attracted considerable attention in the field of high-performance materials [1]. They consist of at least four to five principal elements occuring in an equimolar or near equimolar ratio, such that their fractions do not drop below 5 % or exceed 35 % [2–4]. HEAs owe their name mainly to the large contribution of configurational entropy to the Gibbs free energy. It is supposed that the influence of the entropy stabilizes random solid solutions even at lower temperatures [5, 6]. However, mixing enthalpies and the atomic size mismatches between the components decisively contribute to the phase selection criterion at lower temperatures [4] and the formation of secondary phases can often not be completely avoided [7].

The interest in high-entropy alloys is mostly triggered by their outstanding mechanical properties, making them alternatives for certain superalloys or metallic glasses [2, 4, 8–16]. However, high-entropy alloys are not only characterized by a large configurational entropy, but also by high atomic-level stresses arising from local lattice distortions due to atomic size differences [17]. It has been reported that structural and chemical disorder affect both defect kinetics and heat dissipation, which is of particular interest in the context of radiation resistant materials [18]. Recent molecular dynamics (MD) simulations revealed that defect concentrations can be significantly reduced during irradiation in equiatomic multicomponent alloys as compared to elemental metals [19, 20]. This advantageous robustness against radiation damage can be ascribed to a reduced defect mobility and consequently a smaller growth rate of defect clusters [19–21]. Additionally, chemical disorder decreases thermal conductivity, which is also assumed to prevent the formation of large defect clusters by facilitating defect annihilation [17, 18, 22]. If, on the other hand, a HEA has a tendency towards multiphase formation at lower temperatures, particle irradiation can also drive the system into thermodynamic equilibrium and lead to precipitiation [21]. Thus, in irradiated high-entropy alloys there is a delicate interplay of thermodynamic driving forces due to configurational entropy, mixing/demixing tendencies, and irradiation-induced far-from-equilibrium conditions.

The objective of the present study is to address this issue in a four-component CuNiCoFe alloy in thermodynamic equilibrium and under particle irradiation, as well as to study the transition from a single phase HEA to multiphase or so-called compositionally complex alloy. Using a hybrid simulation scheme consisting of alternating Monte-Carlo (MC) and MD steps, we start by generating a model alloy which is truly stabilized by configurational entropy at elevated temperatures. We then show that this structure decomposes at lower temperatures by precipation of small copper clusters. Both the high-entropy and the partly decomposed sample are then subjected to a series of 1,500 recoil events and the damage accumulation is analyzed and compared to elemental Ni as reference system. Moreover, we show that segregation effects occur at irradiation-induced defects, promoting the formation of precipitates.

II. METHODS

A. Equilibrium simulations

The embedded atom method [23] was used to describe interatomic interactions in the multicomponent CuNiCoFe alloy system. Parametrizations for the elemental interactions were taken from Zhou *et al.* [24]. The miss-

ing cross terms were created using the potential generator from the same authors, which is based on a single element mixture procedure [24]. Initially, atoms were distributed randomly on a regular FCC lattice of about $N = 100,000$ sites, such that an equimolar configuration was obtained. We applied 3-dimensional periodic boundary conditions and the initial lattice constant was approximated according to Vegard's law [25]. After the construction of the initial structure, we minimized its free energy with a mixed MC/MD procedure, carried out using the open source code LAMMPS [26]. For the MC steps, we used the variance-constrained semi-grand-canonical (VC-SGC) ensemble [27]. This ensemble is based on the semi-grand-canonical ensemble with an added constraint on the overall composition. Thus, it resembles a canonical ensemble, but allows Gaussian variations of the concentration, the extent of which is controlled by the parameter κ. We chose a value of $\kappa = 10^3$ in our simulations. The VC-SGC ensemble allows simulations inside miscibility gaps and has a performance advantage over the canonical ensemble, which cannot be parallelized easily [27]. The miscibility is controlled via the chemical potential differences. The chemical potential differences with regard to copper were determined as $\Delta\mu_{\text{Cu–Ni}} = 0.9\,\text{eV}$, $\Delta\mu_{\text{Cu–Co}} = 0.85\,\text{eV}$, and $\Delta\mu_{\text{Cu–Fe}} = 0.7\,\text{eV}$ as described in Ref. 28. The values at hand lead to a miscible CuNiCoFe system at 800 K.

The MC/MD simulations were performed at different target temperatures $T = 800\,\text{K}, 750\,\text{K}, \ldots, 400\,\text{K}$, with $N/4$ MC trial moves followed by 20 MD steps. For the MD steps, we used a timestep of 1 fs, as well as a Nosé–Hover thermostat and a Parinello–Rahman barostat at temperature T and ambient pressure. In total, the simulations were run for $1,000,000$ MD steps (including $50,000$ MC cycles), after which the potential energy was definitely converged.

B. Irradiation simulations

We simulated irradiation of the structures using the approach introduced in Ref. 19 with the PARCAS MD code [29]. Simulations were started from either pure Ni, a CuNiCoFe cell with random element distribution, or the equilibrated sample from the MC/MD run at 400 K. After equilibration at room temperature to zero pressure, the simulation cell size was fixed and a series of subsequent 5 keV recoils was initiated in the cell. The recoils were performed by assigning a velocity vector with a magnitude corresponding to the recoil energy and a random direction to the atom closest to the center of the simulation cell. Each recoil was simulated for 30 ps, which was sufficient to cool the cell back down to ambient temperature by Berendsen temperature scaling [30] in a thin layer at the simulation box boundaries. After this, all atom coordinates were shifted by a displacement vector with components randomly selected in the interval $[0, L_d]$, where L_d is the cell size in each of the 3 dimensions d. After the shift, atoms outside the boundaries were wrapped back into the cell according to the periodic boundary conditions. This procedure ensures homogeneous irradiation of the entire simulation cell. Experimentally, this is comparable, e.g., to prolonged neutron or high-energy ion irradiation of a segment inside the material.

The irradiation simulations used the same interatomic potential as the MC/MD simulations, except that for small interatomic separations (well below the equilibrium nearest-neighbor distance) the potentials are smoothly joint to the universal repulsive Ziegler–Biersack–Littmark (ZBL) interatomic potential [31]. The ZBL-96 electronic stopping [32] was applied on all atoms with kinetic energies higher than 10 eV. Monitoring of the simulations showed that about 20 % of the initial recoil energy was lost to electronic stopping, i.e., the nuclear deposited damage energy per recoil is about 4 keV. The total deposited nuclear energy was extracted by summing up the damage energies and then used to calculate the displacements-per-atom (dpa) value, a standard unit for radiation damage exposure [33, 34]. This irradiation simulation approach has previously been demonstrated to lead to a good agreement with experiments on other HEAs [19, 35].

C. Analysis of short-range order and lattice defects

In order to quantify the chemical ordering, we used the Warren–Cowley short-range order (SRO) parameters α_1 and α_2 adapted to a multicomponent alloy [36]

$$\alpha_n^{ij} = 1 - \frac{P_n^{ij}}{c_j}, \tag{1}$$

where the subscript $n \in \{1, 2, \ldots\}$ refers to the n^{th} coordination sphere, P_n^{ij} describes the conditional probability of an atom of type j being adjacent to an atom of type i, and c_j is the concentration of atom type j. A Warren–Cowley parameter of zero represents the case of an ideal solid solution with no tendency for clustering. Ordered structures (attractive SRO) can be assumed if α is positive, while negative values reflect preferences for segregation (repulsive SRO). We calculated the SRO parameters for the equilibrium structures as a time average over 20 snapshots taken during 2000 simulation steps. Those snapshots were minimized prior to analysis to remove thermal fluctuations and to obtain the 0 K ground-state values. For the irradiated cells, the SRO analysis was performed in the same manner, except that averaging was only performed where noted.

We used the open source application OVITO [37] for the analysis and visualization of simulation results: Atomic volumes were calculated by Voronoi tesselation of minimized samples [38–41], defective atoms were marked by common neighbor analysis (CNA) with an adaptive cutoff [42, 43], and dislocation lines were identified using

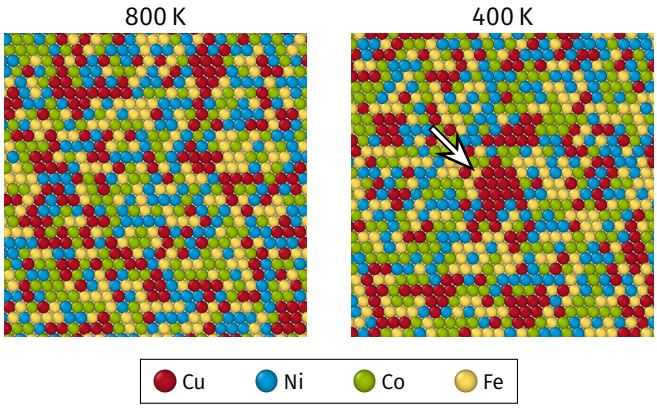

FIG. 1. Snapshots of the CuNiCoFe alloy, equilibrated in the VC-SGC ensemble at 800 K (left) and 400 K (right). The arrow highlights a clustering of copper atoms, indicating that phase separation occurs at lower temperatures.

the dislocation extraction algorithm (DXA) [44]. Additionally, we also performed a Wigner–Seitz cell defect analysis [45]. This analysis constructs the space-filling Wigner–Seitz cells of the perfect underlying FCC lattice, labeling empty cells as vacancies and doubly-filled ones as interstitials. Since this analysis is space-filling, it gives a definite determination of whether a defect region is of vacancy or interstitial type (complex defects may involve both, but then the difference in the number of vacancies vs. interstitials of the same cluster determines its character [46]). The supplemental information provided by this analysis helps to identify point defects, which cannot be treated by DXA.

III. RESULTS AND DISCUSSION

A. CuNiCoFe in thermodynamic equilibrium

Figure 1 shows the final structures after equilibration in the VC-SGC ensemble at 800 K (left) and at 400 K (right). The configurations differ slightly in their atomic arrangement. Whereas Cu (red atom type) is randomly distributed at 800 K, it tends to form small clusters in the structure at 400 K, indicated by the white arrow. The Warren–Cowley parameters at both temperatures are shown in Fig. 2. All α_n values more or less deviate from the ideal solid solution in either the positive or negative direction. This behavior is most pronounced for Cu. On average we find a Warren–Cowley parameter for Cu–Cu of -0.15 for the first neighbor shell at 800 K, indicating a slight tendency to form small Cu clusters (positive ΔH_{mix}). Accordingly, all other $\alpha_1^{\mathrm{Cu}-j}$ values are positive. Except for Fe–Fe interactions, all remaining parameters are slightly negative, indicating miscibility of Ni, Co, and Fe. The α_2 parameter exhibits no strong indication for medium-range ordering at 800 K.

If we repeat the analysis in the same sample equilibrated at 400 K, we see that the ordering tendencies become more distinct and extend into the second neighbor shell. Although the Warren–Cowley parameters for non-Cu pairs also change in magnitude, they still indicate an approximately random solid solution of Co, Ni, and Fe without any remarkable clustering. This can also be inferred from the snapshots in Figure 1. Figure 2c further shows that the Cu segregation tendencies increase nonlinearly with decreasing temperature. Note that we do not observe any structural phase transitions, such as a transition from an FCC to a BCC lattice or even amporphization.

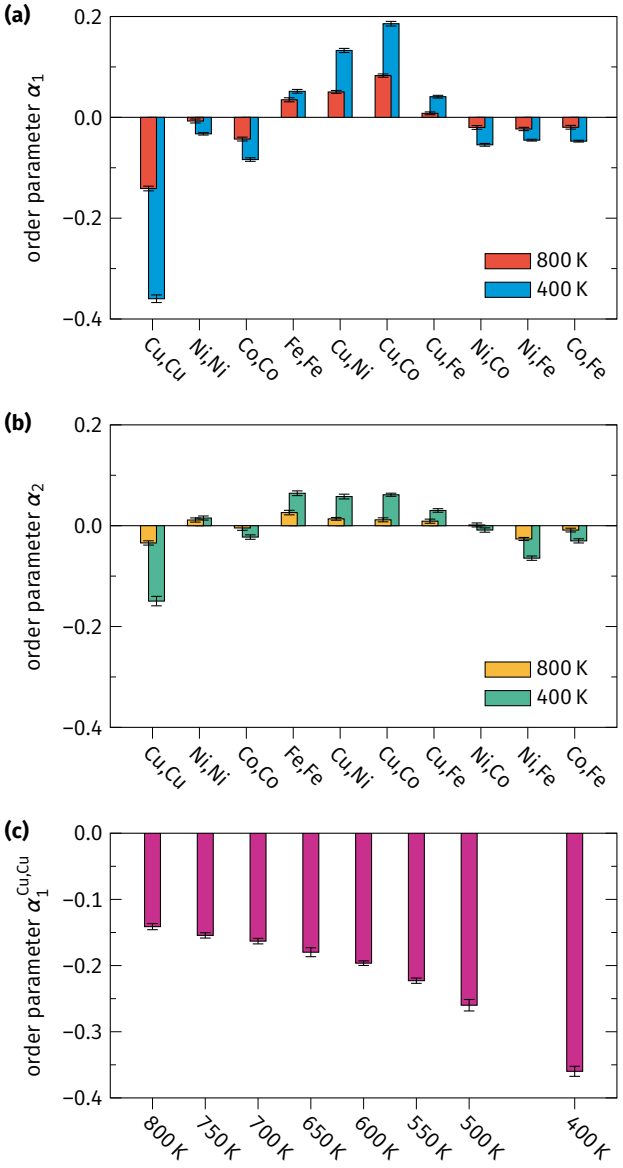

FIG. 2. Warren–Cowley parameters α_1 (a) and α_2 (b) for the CuNiCoFe alloy system at 800 K and 400 K. (c) The change of $\alpha_1^{\mathrm{Cu,Cu}}$ with temperature. Increasing Cu–Cu ordering tendencies can be observed with decreasing temperature. All values are averaged over 20 snapshots at 0 K, with the error bars representing the standard deviation.

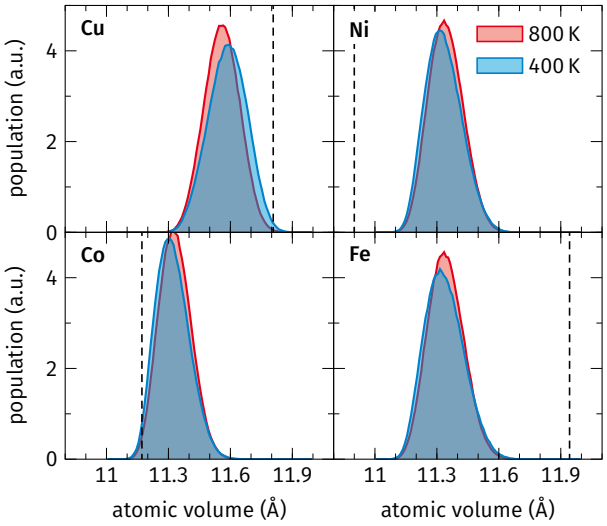

FIG. 3. Comparison of the atomic volumes at 0 K for the HEA equilibrated at 400 K (red) and 800 K (blue). The dashed lines indicate the ground state atomic volume of the single-element FCC structures. Atomic volumes are obtained from Voronoi tesselation of 20 snapshots at 0 K.

These results may be interpreted as follows: The contribution of the configurational entropy at 400 K is insufficient to compete against the enthalpy of mixing. Since the composition of the system is fixed, it will demix by locally forming copper-rich clusters. When decreasing the temperature in experiment, there is a competition between the increasing thermodynamic driving force for decomposition and the decreasing diffusivity within the system. For this reason, HEAs very often represent kinetically trapped metastable configurations at lower temperatures and local segregation occurs as an ageing phenomenon.

When comparing the atomic volumes as a function of the atom type (see Fig. 3), it can be seen that Cu has slightly larger values than Co, Ni, or Fe. Both Ni and Co possess higher atomic volumes in the multicomponent system than in their elemental state. In contrast, Cu and Fe exhibit smaller atomic volumes compared to their pure structures. At 400 K, the system starts demixing into a ternary Co, Ni, and Fe solid solution and into a copper-rich phase. The copper atoms expand slightly, while the ternary solid solution becomes slightly denser. This brings Cu, Co, and Ni closer to their preferred atomic volume. Only Fe deviates from this trend, but exhibits a positive Warren–Cowley parameter, indicating a preference for unlike neighbors. This changed chemical environment may influence the equilibrium volume.

In summary, these observations suggest that the small scale decomposition is driven largely by the mixing enthalpy at low temperatures, but additionally enhanced by atomic size effects.

B. Irradiation

Thus far, we studied the thermodynamic stability of a CuNiCoFe solid solution. In section III A, we demonstrated by means of hybrid MC/MD simulations that CuNiCoFe exhibits a tendency for decomposition at lower temperatures (400 K). These results suggest that in this case a random distribution is only stabilized by kinetic inhibition. In the following, we will therefore discuss the effect of cascade events on the evolution of the chemical order, focusing on the question, if the energy that is released during recoil events enables the decomposition of Cu. Additionally, we investigate the structural damage due to irradiation by comparison with a Ni sample.

1. *Lattice defects*

Earlier work comparing irradiation damage in elemental metals and disordered alloys suggests that the FCC structure is retained throughout irradiation with 1,500 recoils [19]. Figure 4(a) shows that this is also the case for the initially ordered HEA sample (equilibrated with MC/MD at 400 K). Since the structural damage in the initially random HEA is similar, we omit this sample from the discussion at hand. For comparison, Figure 4(b) shows a pure Ni reference sample which underwent the same irradiation treatment. Most irradiation damage in these samples manifests itself by the formation of dislocation loops, stacking-fault tetrahedra, and single vacancies or vacancy clusters. Vacancy clusters and extended defect agglomerates cannot be identified by the DXA and are indicated by red defect meshes. A visualization of atom positions in Fig. 4c reveals that these regions are dominantly characterized by vacant lattice sites. The nature of these regions has also been confirmed by a Wigner–Seitz cell defect analysis, which shows that the positions of the distorted regions generally coincide with vacancy-type defect clusters (see videos `cascade-CuNiCoFe.mp4` and `cascade-Ni.mp4` in the supplemental material [47]). These vacancy-type defects are homogeneously distributed within the structure.

The irradiation process and therefore the formation and evolution of defects can be divided into three stages. Figures 4a and b visualize one representative configuration for each of the three stages. Figure 4d depicts the defect concentration as a function of the irradiation dose. Initially, the HEA shows a higher defect accumulation than the pure Ni system, which could be caused by higher atomic level stresses within the multicomponent system. This results in a reduced defect formation energy and thus increased number of defects[17]. In turn, pure Ni exhibits a higher recombination rate due to an increased point defect mobility [18, 22], which means that fewer defects are created per recoil event. During the first cascades, mainly point defects occur in both structures, while the concentration of dislocation-network-like structures is still small.

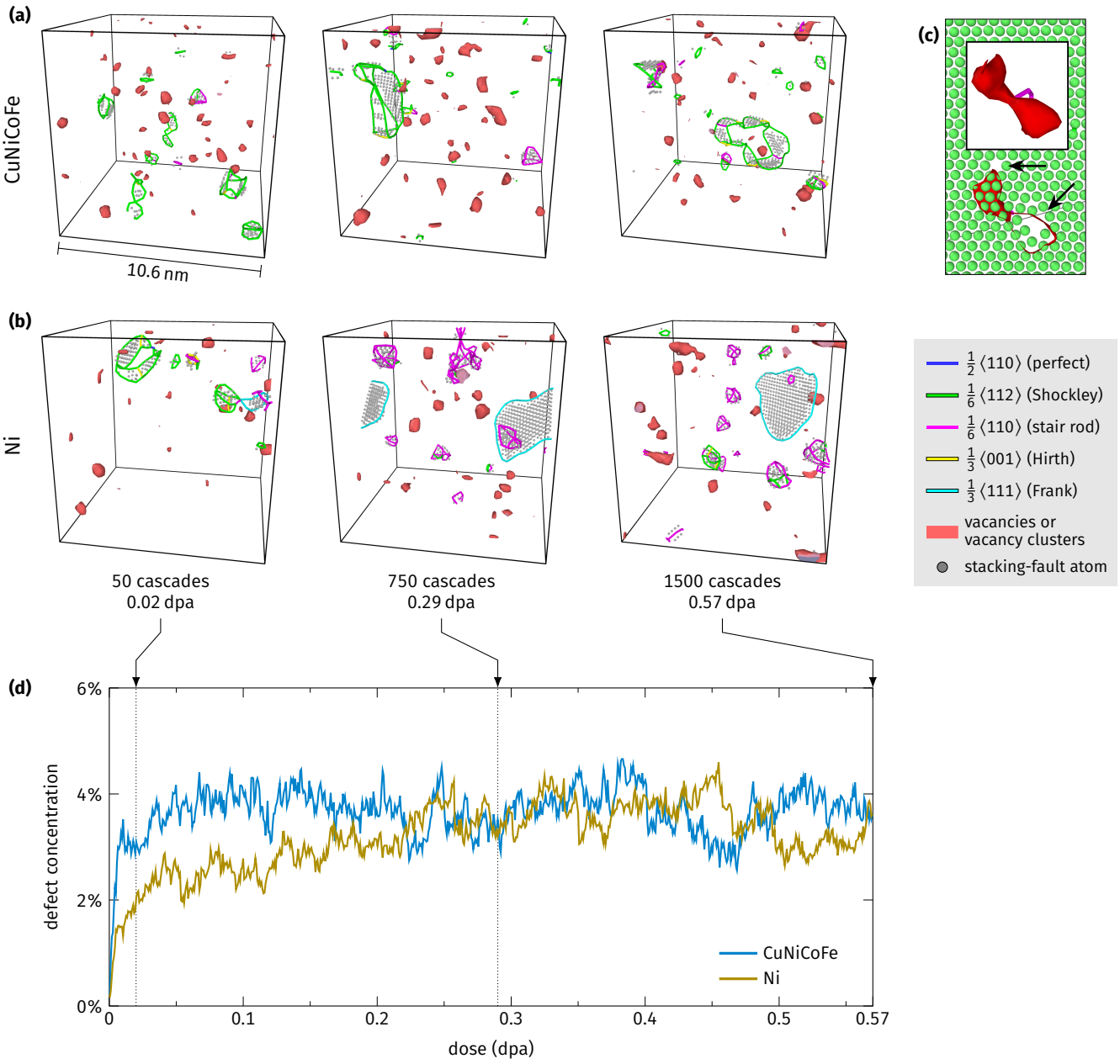

FIG. 4. Analysis of the build-up of lattice defects during irradiation. (a) DXA analysis of the initially ordered HEA at different irradiation doses. (b) The same for a Ni sample. Empty space represents the perfect FCC lattice; the structures do not collapse during irradiation. Green lines indicate ⟨112⟩ partial dislocations, turquoise lines indicate a Frank loop, purple lines belong to stacking fault tetrahedra, and red surfaces enclose defects that cannot be recognized by DXA. Videos of these simulations can be found in the supplemental material [47] (`CuNiCoFe-ordered-DXA-during-irradiation.mp4` and `Ni-DXA-during-irradiation.mp4`). (c) A closer look at those red regions reveals that they represent vacancies and vacancy clusters. In (d), a plot of the concentration of defective atoms as identified by CNA is shown as a function of the irradiation dose. In agreement with the DXA results, we can see that the HEA quickly reaches a high defect concentration that saturates around 4 %. These defects consist mostly of vacancies and small dislocation networks. Pure Ni builds up the defect concentration more slowly. At first—similar to the HEA—vacancies and small dislocation networks appear, then these start disappearing in favor of stacking-fault tetrahedra and a Frank loop.

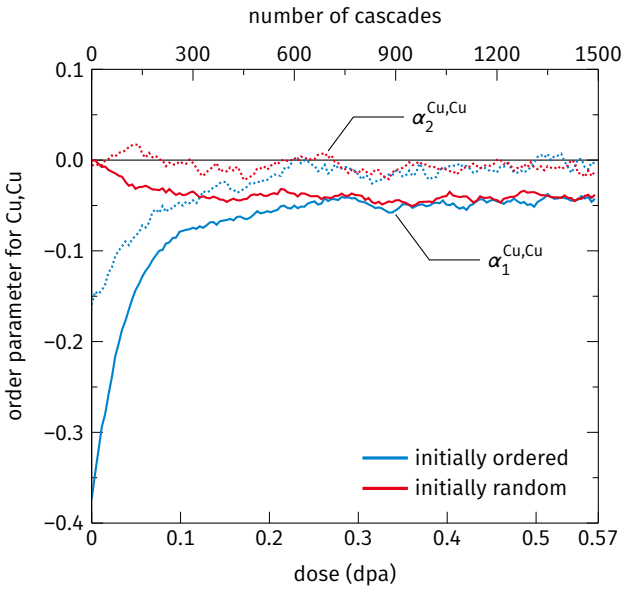

FIG. 5. Evolution of the SRO during irradiation. Only the Cu–Cu parameters are shown, the graphs for all parameters can be found in Fig. S1 in the supplemental material [47]. The sample which was equilibrated using VC-SGC (blue) and the one which was initially random (red) converge to the same values for the order parameters.

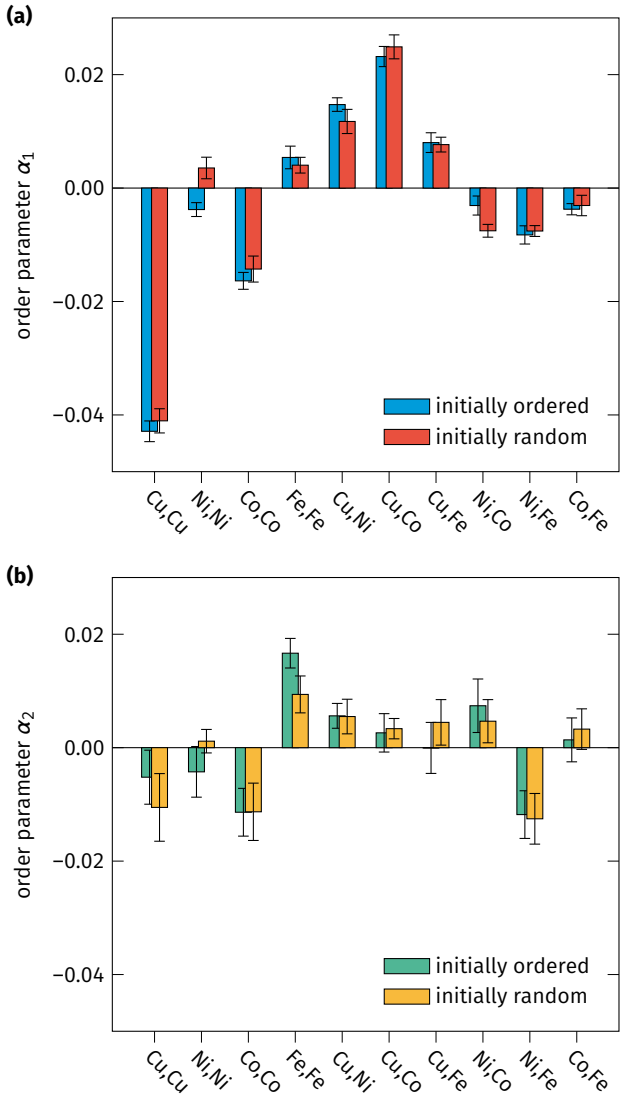

FIG. 6. Final order parameters for the first (a) and second neighbor shell (b) after irradiation with a dose of 0.57 dpa. The values are averaged over the last 10 frames of the irradiation simulation, with the error bars representing the standard deviation.

In the second stage, with an increase of irradiation damage, the defect concentration in pure Ni increases and reaches the same magnitude as in the high-entropy structure. It can be seen that apart from vacancies and stacking-fault tetrahedra, a rather large and stable dislocation loop is formed by the agglomeration of small defects during successive cascades. In general, the rate of defect annihilation depends on both the size and the spatial distribution of the defects. Small defects can be annihilated if they are hit by a single recoil event, while larger defect structures are not engulfed completely and are therefore more stable. Furthermore, the agglomeration of defects in Ni leads to their localization, while the small defects in the HEA are more homogeneously distributed. This means that the probability of a cascade randomly hitting a defect is higher in the HEA and a steady state of annihilation and creation is reached (see video `cascade-CuNiCoFe.mp4` in the supplemental material [47]). A small number of stacking-fault tetrahedra appear, but seem to be unstable. Additionally, we can observe the formation of complex networks of partial dislocations. Because of the large amount of dislocation junctions, these networks must be sessile. Thus, large movements of these networks must again be a series of annihilation and creation events, and they are therefore also unstable against irradiation. In Ni, the defects are assimilated into larger structures, such as sessile Frank dislocation loops, before they can be destroyed by the next cascade (see the video `cascade-Ni.mp4` in the supplemental material [47], starting at 0:40; defect close to the center of the box). As such, Ni possesses a higher volume fraction of undisturbed lattice in which the net defect creation rate is always positive. Additionally, in contrast to the HEA, the stacking-fault tetrahedra are numerous.

In the final stage, we also observe a saturation of the defect concentration in pure Ni, while maintaining the steady state in the alloy system. The development of a steady state in the elemental structure is contrary to earlier publications [20], where a continuous growth of defect networks has been detected. The reason for a reduced growth rate of defect concentrations in Ni is a simulation size effect [48], since the earlier simulation used larger simulation cells compared to the current work.

In order to examine the stability of the lattice de-

fects in the absence of irradiation, an MD simulation at 800 K for 1 ns was performed for the initially ordered HEA. The results reveal neither large movement nor creation or dissolution of a significant number of defects, which indicates that the defects are stable and sessile even at elevated temperatures (see video `reanneal-irradiated-CuNiCoFe.mp4` in the supplemental material [47]).

2. *Chemical order*

In the following we analyze whether high energy recoils are able to initiate local segregation processes, or if the SRO remains more or less constant after every subsequent cascade. Again, we use the Warren-Cowley parameters $\alpha_{1,2}^{ij}$ for the first and second neighbor shell to quantify the extent of atomic clustering. Figure 5 shows $\alpha^{\mathrm{Cu,Cu}}$ for two cells: the HEA with initially random atom distribution, and the HEA after MC/MD at 400 K which shows segregation tendencies for Cu. The analysis is limited to atoms in perfect FCC environments and therefore excludes atoms in defective sites introduced by the irradiation. Order parameters for pairs other than Cu–Cu are plotted in Fig. S1 in the supplemental material [47]. We find that the order parameter $\alpha_1^{\mathrm{Cu,Cu}}$, although exhibiting initial partial segregation in the structure pre-ordered by MC/MD, eventually converges to small negative values. The initially random structure converges to the same value. Mid-range order is always disturbed by irradiation: the parameter $\alpha_2^{\mathrm{Cu,Cu}}$ converges to zero in both cases. This shows that the cascade has two counteracting effects: Firstly, it locally activates the thermodynamically preferrable segregation of Cu. Secondly, it concurrently randomizes the element distribution. The resulting steady state is reached after approximately 700 cascades.

Figure 6 shows the comparison of the Warren-Cowley parameters $\alpha_{1,2}$ for all pairs in the CuNiCoFe alloy for both structures (pre-ordered and fully random) after the full irradiation dose. Comparing these results to those in Fig. 2 (note the scale difference in the y axes), we observe that the absolute values of both parameters α_1 and α_2 are reduced by roughly one order of magnitude due to the irradiation. Importantly, after irradiation all pairs have practically the same α parameters regardless of the initial state. We also note that the α_2 values are consistently smaller than the α_1, indicating that the ordering effects under irradiation are limited to the nearest-neighbor shell.

Based on this analysis, we conclude that while collisional cascades provide activation energy for demixing, the system is dynamically driven to a mostly random steady state, independent of the initial chemical order.

TABLE I. Composition inside defects of the irradiated sample before and after an additional, subsequent MC/MD run. Irradiated sample averaged over 50 snapshots (500 cascades). Note that the total composition of the sample stays equimolar during MC/MD because of the variance constraint and that the composition on the intact lattice sites also stays roughly equimolar because of the comparatively low amount of defect sites.

element	composition after irradiation	composition after subsequent MC/MD
Cu	26.9%	49.4%
Ni	24.9%	17.1%
Co	23.3%	14.0%
Fe	24.9%	19.5%

IV. POST-IRRADIATION EFFECTS

Thermodynamic equilibration of a four-component CuNiCoFe alloy with a perfect FCC lattice showed a segregation tendency for Cu atoms. From the results of Sec. III A we can assume that there is not only a chemical but also a sterical driving force for Cu to segregate from the solid solution into small clusters. We already concluded that the growth of Cu clusters is accompanied by an increasing Cu atomic volume. Nevertheless, thus far, we mainly concentrated on the thermodynamics of the defect-free system. Therefore, we again ran hybrid MC/MD simulations in the VC-SGC ensemble. However, this time, the irradiated sample with pre-existing defects was taken as a starting configuration. Table I lists the composition inside the lattice defects. Obviously, defect sites that offer excess volume serve as sinks for Cu atoms and even enhance the amount of segregated Cu after equilibration. In this regard, the presence of defects enhances the driving force for local decomposition. Within the defects, we can find a Cu proportion which is approximately 50 %. In contrast, during the irradiation the distribution of Cu atoms does not alter significantly. In Fig. 7 we visualized the atoms located within the defect structure before (left) and after (right) the equilibration. Copper atoms are displayed with a red color, while all others are shown in gray. Figures 7c and d highlight two defects separately. From these illustrations we draw the conclusion that Cu preferentially segregates on, e.g., the edges of stacking-fault tetrahedra rather than in the stacking faults themselves. The reason lies in the higher local excess volume of these sites (cf. Fig. 3).

In conclusion, all results suggest that the mixing enthalpy of Cu is the decisive factor for phase stability in this case, exceeding the total entropy with decreasing temperature. The limited segregation tendencies of the perfect crystal are surpassed in the presence of defects, which act as sinks for copper.

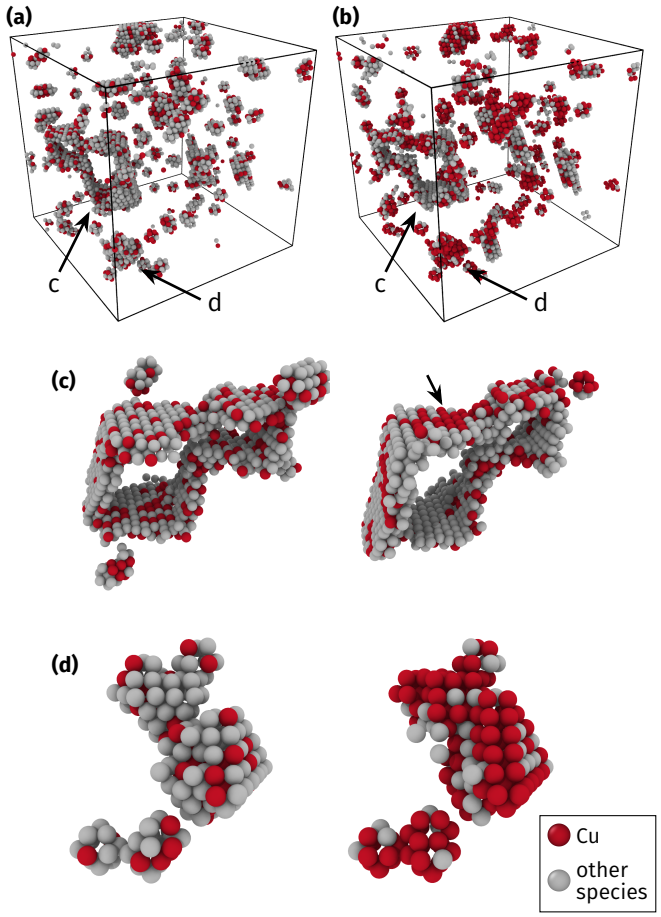

FIG. 7. VC-SGC simulations of the HEA sample after irradiation. (a) Atoms identified as defective by CNA after irradiation [same structure as the righmost snaphost in Fig. 4(a)]. Copper atoms are shown in red, all others in gray. (b) The same after subsequent simulation in the VC-SGC ensemble. The concentration of copper atoms around the defects is highly increased. Detailed views of a dislocation structure (c) and a stacking-fault tetrahedron (d) are provided.

V. CONCLUSION

Using a model CuNiCoFe HEA with a tendency for copper segregation, we observe that the system reaches a steady state of defect concentration and of chemical order under irradiation, irrespective of the initial structure. In contrast to pure metals, irradiation leads to less mobile point defects and therefore a larger number of isolated defects instead of recombination or agglomeration. While, e.g., Ni increases its defect concentration continuously with increasing irradiation dose due to the agglomeration of defects in larger, more stable structures, the HEA quickly reaches a steady state of defect creation and annihilation. Irradiation provides the thermal activation for demixing of copper, but at the same time re-randomizes the elemental distribution. The resulting steady state of chemical order is close to a random solid solution, but still shows traces of local precipitation. Furthermore, our simulations reveal that various lattice defects act as sinks for copper, most likely since the copper atoms are the largest species and the defects provide excess volume. This clustering of copper at defects is also suppressed during irradiation for the reasons enumerated above. Together, these effects explain the high irradiation resistance of HEAs.

ACKNOWLEDGMENTS

The authors gratefully acknowledge travel grants through the PPP Finland program of the Deutscher Akademischer Austauschdienst (DAAD). Computing time was made available by the Technische Universität Darmstadt on the Lichtenberg cluster and the IT Center for Science, CSC, Finland.

* koch@mm.tu-darmstadt.de

[1] Z. Wang, S. Guo, and C. T. Liu, "Phase selection in high-entropy alloys: From nonequilibrium to equilibrium," JOM **66**, 1966–1972 (2014).
[2] Y. F. Ye, Q. Wang, J. Lu, C. T. Liu, and Y. Yang, "High-entropy alloy: challenges and prospects," Mater. Today **19**, 349–362 (2016).
[3] F. Otto, Y. Yang, H. Bei, and E. P. George, "Relative effects of enthalpy and entropy on the phase stability of equiatomic high-entropy alloys," Acta Mater. **61**, 2628–2638 (2013).
[4] E. J. Pickering and N. G. Jones, "High-entropy alloys: a critical assessment of their founding principles and future prospects," Int. Mater. Rev. **61**, 183–202 (2016).
[5] C. C. Tasan, Y. Deng, K. G. Pradeep, M. J. Yao, H. Springer, and D. Raabe, "Composition dependence of phase stability, deformation mechanisms, and mechanical properties of the CoCrFeMnNi high-entropy alloy system," JOM **66**, 1993–2001 (2014).
[6] J.-W. Yeh, "Alloy design strategies and future trends in high-entropy alloys," JOM **65**, 1759–1771 (2013).
[7] M. Widom, W. P. Huhn, S. Maiti, and W. Steurer, "Hybrid Monte Carlo/molecular dynamics simulation of a refractory metal high entropy alloy," Metall. Mater. Trans. A **45**, 196–200 (2014).
[8] M.-H. Tsai and J.-W. Yeh, "High-entropy alloys: A critical review," Mater. Res. Lett. **2**, 107–123 (2014).
[9] W. H. Liu, Y. Wu, J. Y. He, Y. Zhang, C. T. Liu, and Z. P. Lu, "The phase competition and stability of high-entropy alloys," JOM **66**, 1973–1983 (2014).
[10] L. Xie, P. Brault, J.-M. Bauchire, A.-L. Thomann, and L. Bedra, "Molecular dynamics simulation of clusters and thin film growth in the context of plasma sputterin deposition," J. Phys. D: Appl. Phys. **47**, 224004 (2014).
[11] F. Tian, L. K. Varga, N. Chen, L. Delczeg, and L. Vitos, "*Ab initio* investigation of high-entropy alloys of 3*d*

elements," Phys. Rev. B **87**, 075144 (2013).
[12] S.-W. Kao, J.-W. Yeh, and T.-S. Chin, "Rapidly solified structure of alloys with up to eight equal-molar elements—a simulation by molecular dynamics," J. Phys: Condens. Matter **20**, 145214 (2008).
[13] A. Haglund, M. Koehler, D Catoor, E. P. George, and V. Keppens, "Polycrystalline elastic moduli of a high-entropy alloy at cryogenic temperatures," Intermetallics **58**, 62–64 (2015).
[14] F. Tian, L. Delczeg, N. Chen, L. K. Varga, J. Shen, and L. Vitos, "Structural stability of $NiCoFeCrAl_x$ high-entropy alloy from *ab initio* theory," Phys. Rev. B **88**, 085128 (2013).
[15] S. Guo, Q. Hu, C. Ng, and C. T. Liu, "More than entropy in high-entropy alloys: Forming solid solutions or amorphous phase," Intermetallics **41**, 96–103 (2013).
[16] C. Ng, J. Luan, Q. Wang, S. Shi, and C.T. Liu, "Phase stability and tensile properties of Co-free $Al_{0.5}CrCuFeNi_2$ high-entropy alloys," J. Alloys Compd. **584**, 530–537 (2014).
[17] T. Egami, W. Guo, P. D. Rack, and T. Nagase, "Irradiation resistance of multicomponent alloys," Metall. Mater. Trans. A **45**, 180–183 (2014).
[18] Y. Zhang, G. M. Stocks, K. Jin, C. Lu, H. Bei, B. C. Sales, L. Wang, L. K. Béland, R. E. Stoller, G. D. Samolyuk, M. Caro, A. Caro, and W. J. Weber, "Influence of chemical disorder on energy dissipation and defect evolution in concentrated solid solution alloys," Nat. Commun. **6**, 8736 (2015).
[19] F. Granberg, K. Nordlund, M. W. Ullah, K. Jin, C. Lu, H. Bei, L. M. Wang, F. Djurabekova, W. J. Weber, and Y. Zhang, "Mechanism of radiation damage reduction in equiatomic multicomponent single phase alloys," Phys. Rev. Lett. **116**, 135504 (2016).
[20] F. Granberg, F. Djurabekova, E. Levo, and K. Nordlund, "Damage buildup and edge dislocation mobility in equiatomic multicomponent alloys," Nucl. Inst. Meth. Phys. Res. Sec. B. **393**, 114–117 (2017).
[21] T. Yang, S. Xia, S. Liu, C. Wang, S. Liu, Y. Fang, Y. Zhang, J. Xue, S. Yan, and Y. Wang, "Precipitation behavior of $Al_xCoCrFeNi$ high entropy alloys under ion irradiation," Sci. Rep. **6**, 32146 (2016).
[22] M. W. Ullah, D. S. Aidhy, Y. Zhang, and W. J. Weber, "Damage accumulation in ion-irradiated Ni-based concentrated solid-solution alloys," Acta Mater. **109**, 17–22 (2016).
[23] S. M. Foiles, M. I. Baskes, and M. S. Daw, "Embedded-atom-method functions for the fcc metals Cu, Ag, Au, Ni, Pd, Pt, and their alloys," Phys. Rev. B **33**, 7983–7991 (1986).
[24] X. W. Zhou, R. A. Johnson, and H. N. G. Wadley, "Misfit-energy-increasing dislocations in vapor-deposited CoFe/NiFe multilayers," Phys. Rev. B **69**, 144113 (2004).
[25] K. T. Jacob, S. Raj, and L. Rannesh, "Vegard's law: a fundamental relation or an approximation?" Int. J. Mater. Res. **98**, 776–779 (2007).
[26] S. Plimpton, "Fast parallel algorithms for short-range molecular-dynamics," J. Comp. Phys. **117**, 1–19 (1995), `http://lammps.sandia.gov/`.
[27] B. Sadigh, P. Erhart, A. Stukowski, A. Caro, E. Martinez, and L. Zepeda-Ruiz, "Scalable parallel Monte Carlo algorithm for atomistic simulations of precipitation in alloys," Phys. Rev. B **85**, 184203 (2012).
[28] T. Brink, L. Koch, and K. Albe, "Structural origins of the boson peak in metals: From high-entropy alloys to metallic glasses," Phys. Rev. B **94**, 224203 (2016).
[29] K. Nordlund, PARCAS computer code (2016). The main principles of the molecular dynamics algorithms are presented in Refs. 45 and 49. The adaptive time step and electronic stopping algorithms are the same as in Ref. 50. The 2016 version of the code is published in the online supplementary material to Ref. 19.
[30] H. J. C. Berendsen, J. P. M. Postma, W. F. van Gunsteren, A. DiNola, and J. R. Haak, "Molecular dynamics with coupling to an external bath," J. Chem. Phys. **81**, 3684 (1984).
[31] J. F. Ziegler, J. P. Biersack, and U. Littmark, *The Stopping and Range of Ions in Matter* (Pergamon, New York, 1985).
[32] J. F. Ziegler, (1996), SRIM-96 computer code, private communication.
[33] ASTM Standard E693-94, "Standard practice for characterising neutron exposure in iron and low alloy steels in terms of displacements per atom (dpa)," (1994).
[34] K. Nordlund, S. J. Zinkle, T. Suzudo, R. S. Averback, A. Meinander, F. Granberg, L. Malerba, R. Stoller, F. Banhart, B. Weber, F. Willaime, S. Dudarev, and D. Simeone, *Primary radiation damage in materials: Review of current understanding and proposed new standard displacement damage model to incorporate in-cascade mixing and defect production efficiency effects* (OECD Nuclear Energy Agency, Paris, France, 2015) available online at `https://www.oecd-nea.org/science/docs/2015/nsc-doc2015-9.pdf`.
[35] S. Zhang, K. Nordlund, F. Djurabekova, F. Granberg, and T. S. Wang, "Radiation damage buildup by athermal defect reactions in nickel and concentrated nickel alloys," APL Mater. (2016), submitted for publication.
[36] J. M. Cowley, "An approximate theory of order in alloys," Phys. Rev. **77**, 669–675 (1950).
[37] A. Stukowski, "Visualization and analysis of atomistic simulation data with OVITO—the open visualization tool," Model. Simul. Mater. Sci. Eng. **18**, 015012 (2010), `http://ovito.org/`.
[38] G. Voronoï, "Nouvelles applications des paramètres continus à la théorie des formes quadratiques. Premier mémoire. Sur quelques propriétés des formes quadratiques positives parfaites," J. Reine Angew. Math. **133**, 97–102 (1908).
[39] G. Voronoï, "Nouvelles applications des paramètres continus à la théorie des formes quadratiques. Deuxième mémoire. Recherches sur les paralléllоèdres primitifs," J. Reine Angew. Math. **134**, 198–287 (1908).
[40] G. Voronoï, "Nouvelles applications des paramètres continus à la théorie des formes quadratiques. Deuxième mémoire. Recherches sur les paralléllоèdres primitifs. Seconde partie. Domaines de formes quadratiques correspondant aux différents types de paralléloèdres primitifs," J. Reine Angew. Math. **136**, 67–182 (1909).
[41] W. Brostow, M. Chybicki, R. Laskowski, and J. Rybicki, "Voronoi polyhedra and Delaunay simplexes in the structural analysis of molecular-dynamics-simulated materials," Phys. Rev. B **57**, 13448–13458 (1998).
[42] J. D. Honeycutt and H. C. Andersen, "Molecular dynamics study of melting and freezing of small Lennard–Jones clusters," J. Phys. Chem. **91**, 4950–4963 (1987).
[43] A. Stukowski, "Structure identification methods for atomistic simulations of crystalline materials," Model. Simul.

Mater. Sci. Eng. **20**, 045021 (2012).
[44] A. Stukowski, V. V. Bulatov, and A. Arsenlis, "Automated identification and indexing of dislocations in crystal interfaces," Model. Simul. Mater. Sci. Eng. **20**, 085007 (2012).
[45] K. Nordlund, M. Ghaly, R. S. Averback, M. Caturla, T. Diaz de la Rubia, and J. Tarus, "Defect production in collision cascades in elemental semiconductors and fcc metals," Phys. Rev. B **57**, 7556–7570 (1998).
[46] K. Nordlund and F. Gao, "Formation of stacking fault tetrahedra in collision cascades," Appl. Phys. Lett. **74**, 2720–2722 (1999).
[47] See Supplemental Material at [URL will be inserted by publisher] for videos of the irradiation simulations and a figure of the detailed evolution of SRO during irradiation.
[48] E. Levo, F. Granberg, C. Fridlund, K. Nordlund, and F. Djurabekova, "Radiation damage buildup and dislocation evolution in equiatomic multicomponent alloys," J. Nucl. Mater. (2016), submitted for publication.
[49] M. Ghaly, K. Nordlund, and R. S. Averback, "Molecular dynamics investigations of surface damage produced by kiloelectronvolt self-bombardment of solids," Philos. Mag. A **79**, 795–820 (1999).
[50] K. Nordlund, "Molecular dynamics simulation of ion ranges in the 1–100 keV energy range," Comput. Mater. Sci. **3**, 448–456 (1995).

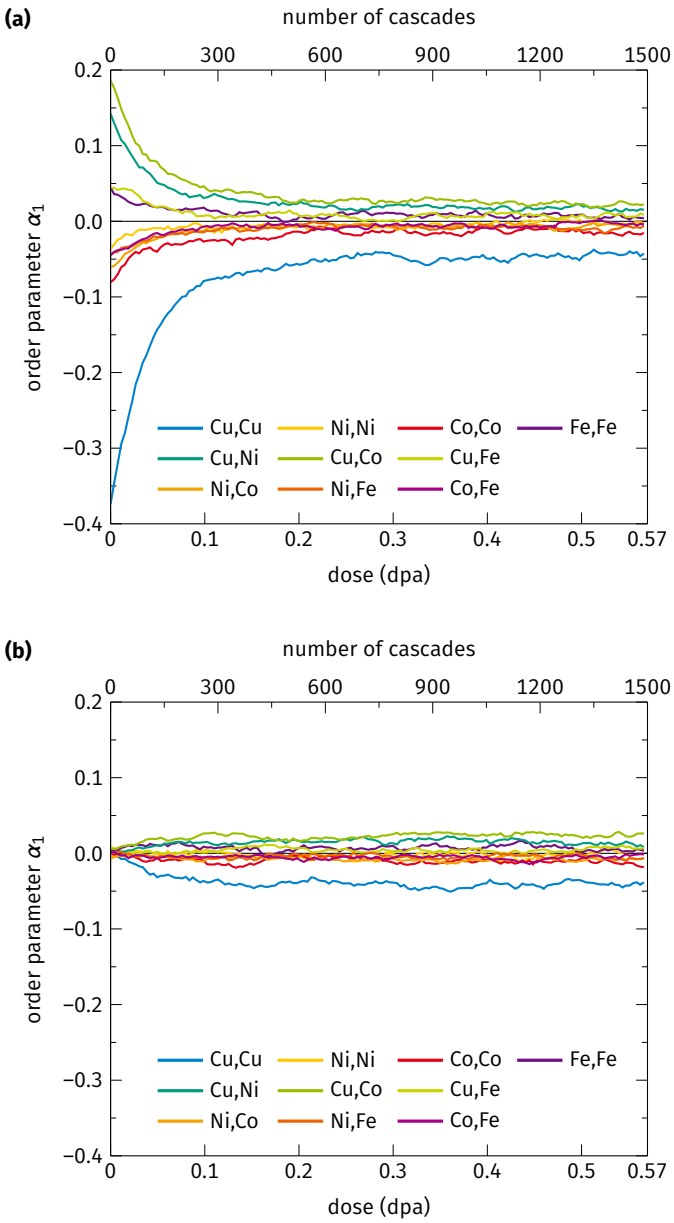

Figure S.1: Evolution of the SRO in CuNiCoFe HEAs during irradiation for all pairs (cf. Fig. 5 in the main paper). (a) Starting from the ordered sample (MC/MD at 400 K). (b) Starting from the initially random sample.